COMPLIMENTARY/POSTER SESSION PAPER

An Adaptable Flying Fish Robotic Model for Aero- and Hydrodynamic Experimentation

Valeria Saro-Cortes [*,1], Yuhe Cui[†], Tierney Dufficy[†], Arsanious Boctor[†], Brooke E. Flammang [‡] and Aimy Wissa[*]

[*]Department of Mechanical and Aerospace Engineering, Princeton University, 26 Olden Street, NJ 08544, USA; [†]Department of Mechanical Science and Engineering, University of Illinois at Urbana-Champaign, 1206 W Green St, IL 61801, USA; [‡]Federated Department of Biological Sciences, New Jersey Institute of Technology, 323 Dr Martin Luther King Jr Blvd, NJ 07102, USA

[1]E-mail: vsarocortes@gmail.com

Synopsis Flying fishes (family *Exocoetidae*) are known for achieving multi-modal locomotion through air and water. Previous work on understanding this animal's aerodynamic and hydrodynamic nature has been based on observations, numerical simulations, or experiments on preserved dead fish, and has focused primarily on flying pectoral fins. The first half of this paper details the design and validation of a modular flying fish inspired robotic model organism (RMO). The second half delves into a parametric aerodynamic study of flying fish pelvic fins, which to date have not been studied in-depth. Using wind tunnel experiments at a Reynolds number of 30,000, we investigated the effect of the pelvic fin geometric parameters on aerodynamic efficiency and longitudinal stability. The pelvic fin parameters investigated in this study include the pelvic fin pitch angle and its location along the body. Results show that the aerodynamic efficiency is maximized for pelvic fins located directly behind the pectoral fins and is higher for more positive pitch angles. In contrast, pitching stability is neither achievable for positive pitching angles nor pelvic fins located directly below the pectoral fin. Thus, there is a clear a trade-off between stability and lift generation, and an optimal pelvic fin configuration depends on the flying fish locomotion stage, be it gliding, taxiing, or taking off. The results garnered from the RMO experiments are insightful for understanding the physics principles governing flying fish locomotion and designing flying fish inspired aerial–aquatic vehicles.

Introduction

The taxonomic family Exocoetidae comprises several genera of flying fish (Fig. 1A), a fish that is unique for its ability to locomote through both air and water. Other animals such as the puffin bird and some squid species are also able to perform their own variations of aerial–aquatic locomotion, but the flying fish particularly excels at having both high speed, highly maneuverable swimming and long distance flight, traveling up to nearly half a kilometer through the air (Siddall and Kovac 2014). The stages of locomotion of the flying fish are described in Fig. 1B, and demonstrate their adeptness in not just swimming underwater, but also gliding through the air and propelling itself along the air–water interface in a process known as "taxi."

Rather than employing entirely different mechanisms for swimming, flying, and taxiing, the fish uses the same anatomical structures differently for each mode of locomotion. In underwater swimming, the flying fish primarily generates thrust with its caudal fin while using its pectoral and pelvic fins to aid in maneuvering. In the air, the fish extends the pectoral and sometimes pelvic fins perpendicular to its body to form lifting surfaces that enable long distance gliding flight (Hertel 1966; Azuma 2006) while the caudal fin is held rigid. The transition from swimming to flying is largely driven by the caudal fin, which launches the fish out of the water, either
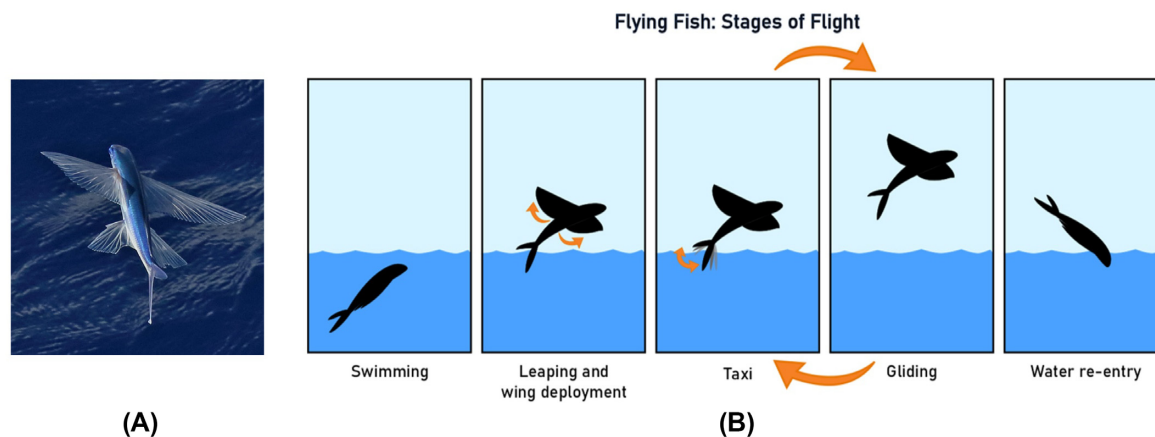
Fig. 1 (A) Photograph of a four-winged flying fish in gliding flight (Kamath 2017). **(B)** The stages of locomotion of a flying fish. When descending from a glide, a flying fish may immediately commence another taxi stage rather than return to fully submerged swimming. This allows it to build back enough speed to take off into gliding again.

directly into gliding flight or into the intermediate taxi stage. In taxi, the caudal fin continues to be used for hydrodynamic thrust generation, while the rest of the fish (i.e., its body and other fins) is above the surface of the water, thus experiencing lower drag compared to underwater locomotion (Fig. 1B-iii) (Breder 1930). The caudal fin continues to propel the fish until enough forward velocity is reached and the fish can take off into a glide. While gliding, when the gliding altitude decreases, the fish may return to the ocean surface and re-submerge only its caudal fin in order to perform taxi again, thus allowing it to regain lost speed and return to the air for another glide. Flying fish have been observed to reach distances of up to 400 m by cycling through gliding and taxi in 50-m bursts (Davenport 1994).

The ability to rapidly change locomotion between air and water makes the flying fish an interesting subject of study in the context of engineering design. However, they are difficult to study because of their complex kinematics, large operation range, and their habitat, which is limited to tropical and subtropical waters (Davenport 1994). As a result, studies on flying fish locomotion dynamics are presently limited. The earliest work describing the behavior and kinematics of the flying fish were field observations performed from boats that succeeded in bringing the strange locomotive patterns of the fish to light in the scientific world, but were riddled with inaccuracies when it came to the specifics of how this locomotion was achieved (Mobius 1885; Durnford 1907; Hankin 1920; Breder 1930). Analytical arguments were later made to establish the validity of the claim that flying fish can fly at all and to estimate performance characteristics of its flight (Fish 1990; Kawachi et al. 1993; Davenport 1994). Some of these disagreements were settled with the advent of stroboscopic filming and by

performing dissections, which confirmed that pectoral fins do not flap during taxi and produced images of the wake of a flying fish in taxi (Edgerton 1941; Franzisket 1965; Davenport 1994). More modern efforts at performing field studies employed acceleration data loggers attached to a specimen, but the fish is believed to have altered its locomotion due to the presence of the data loggers (Makiguchi et al. 2013). To overcome these challenges, some researchers have opted for numerical and lab-based experimental methods. The lift, drag, and pitching moment coefficients of flying fish were first experimentally studied by catching and preserving a flying fish for wind tunnel measurements (Park and Choi 2010). A numerical study of flying fish aerodynamics that allowed more detailed visuals of the flow field was later developed (Deng et al. 2019). However, these more recent computational and experimental studies focused primarily on the effects of the pectoral fins in gliding flight, when some species of flying of fish have been observed to engage both their pectoral and pelvic fins during gliding.

Cypselurus species have been observed to fly with both sets of fins engaged which results in longer distance flights than have been observed for *Exocoetus* species, which only use their pectoral fins in flight and are referred to as "two-winged" fish. Two-winged fish have been observed to reach higher maximum speeds than the *Cypselurus* species, which are referred to as "four-winged" fish (Rayner 1986; Fish 1990). Currently, the impact of the pelvic fins on flying fish aerodynamics has not been studied in depth.

In addition to field experiments or lab experiments on preserved specimens, experimental study of robotic model organisms (RMOs) (Flammang and Porter 2011) provide an alternative strategy to studying organisms.
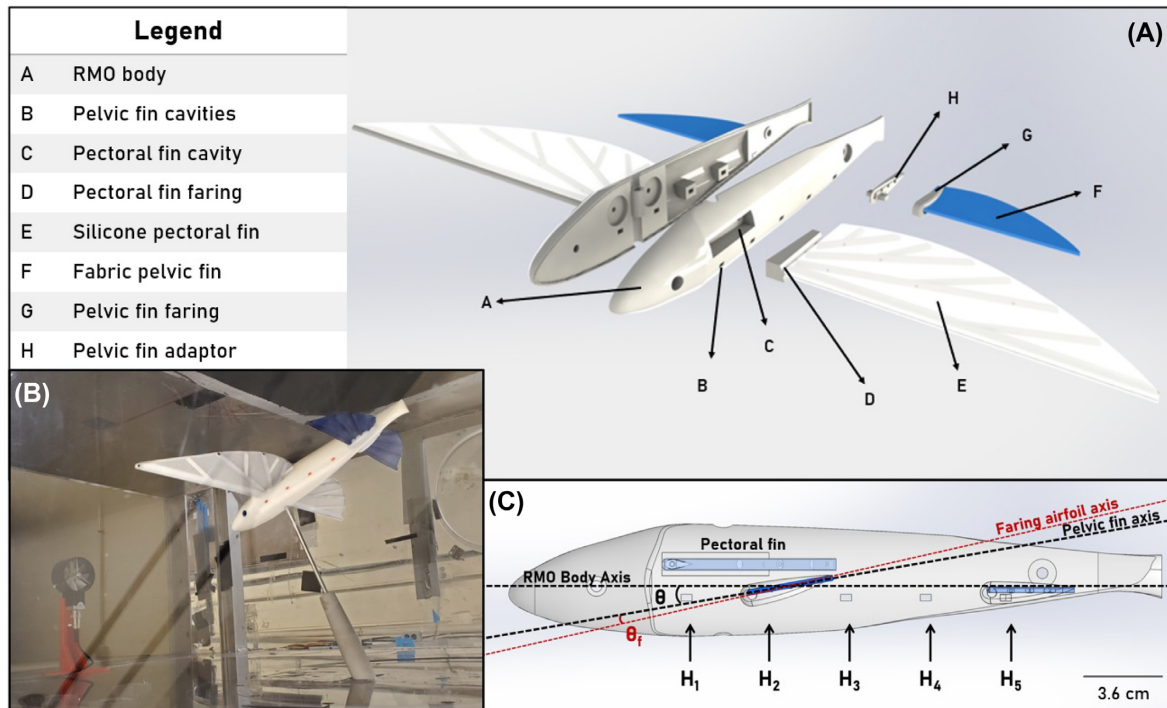
Fig. 2 (A) An exploded view of the aerodynamics platform. **(B)** The RMO is mounted to the wind tunnel on a sting. An anemometer is present to set the fan speed, but it was removed during data collection; **(C)** The pelvic fins on the RMO are designed to be varied by a pitch angle relative to the body axis of the RMO, θ, and a location along the body axis, H_i, where $i = 1, 2, 3, 4$, and 5. Two pelvic fins are shown in the figure to clarify the definition of θ. During the experiment only one pelvic fin was placed on the RMO. A scale bar the length of one pelvic fin mean aerodynamic chord is shown. This is also the the spacing between H_i locations. $\theta_f = 3°$, which is labeled in red, is defined as the angle between the chord line of the airfoil-shaped faring and the pelvic fin fabric. The pectoral fin is highlighted in light blue.

RMOs are designed to be biologically relevant such that biological hypotheses about the corresponding animal can be tested in a controlled laboratory setting. Additionally, RMOs allow researchers to test a larger experimental space than is possible with biological organisms. Researchers can easily change the design and configuration of RMOs, which is not possible for live or dead animals. Thus, RMOs are an invaluable tool for both biologists seeking to understand more elusive mysteries about animal locomotory dynamics as well as engineers looking to nature for design inspiration.

In this paper, we present the design and evaluation of a flying fish RMO. Such an RMO can lend insight into both the existing multi-modal locomotion of the biological flying fish, as well as the design of unmanned aerial–aquatic vehicles (UAAVs) inspired by this locomotion. More specifically, we first present the design, fabrication, and evaluation methods of the RMO components. We then experimentally evaluate the RMO through two case studies to answer the following questions, respectively:

(1) Is the designed RMO biologically relevant, and thus suitable to provide insight about the locomotion of flying fish?

(2) What is the role of the pelvic fin on the aerodynamics of gliding in flying fish and how is this role affected by the pelvic fin parameters?

The answers to the above questions will allow us to fill gaps in the understanding of flying fish aerodynamics. These answers will also aid in forming and testing new hypotheses about the functional morphology of the pectoral and pelvic fins in flying fish. Finally, the parameter space explored in this paper goes beyond what is observable in nature, and thus may be beneficial for exploring evolutionary constraints and designing new engineered vehicles not subject to such constraints.

Design

The design of the flying fish RMO (Fig. 2A) is summarized in this section. The RMO comprises four major components: the body, the pectoral fins, the pelvic fins, and the caudal complex.

Fish body

The fish body profile was similar to that presented in Deng et al. (2019) with some modifications. As many fish bodies are, the profile was streamlined similar to an airfoil (Lucas et al. 2020). From the leading edge of the

pectoral fin to the most posterior end of the fish, the contour was uniform. The uniform contour allowed the pelvic fin adaptors to be attached at any location along the length of the body. The body (Fig. 2A, A) was divided into two halves for ease of assembly. The interior profiles of each body half were lined with tongue and groove structures that meshed together the two pieces.

The body was designed to house the pectoral and pelvic fins. As mentioned previously, the caudal fin was omitted from the prototype because we initially wanted to focus on aerodynamics experiments. Observations of flying fish in gliding flight in previous research show that the caudal fin is held rigid while the fish is in the air (Davenport 1994). Moreover, the thickness of a biological caudal fin is assumed to be negligible and its location downstream of both the pelvic and pectoral fins minimizes the impact of the fin on the fish aerodynamics. Therefore, the fish body was designed for only the pectoral and pelvic fins. A modified body design is needed to incorporate the caudal fin.

As mentioned before, the fish body was designed to allow for modularity of the pelvic fin parameters and to securely mount the pectoral fins. Figure 2A is a schematic of the pectoral and pelvic fins mounted on the RMO with the individual components labeled. To vary the location of the pelvic fin relative to the pectoral fin, H_i, five small rectangular holes were used to mount the pelvic fin at different points along the length of the body. The holes were placed at a ~15 mm vertical distance from the pectoral fin and separated from each other by 36 mm, which is approximately one pelvic fin mean average chord length (Fig. 2C). As for the pectoral fin, it was mounted to the body via a large rectangular cavity located above the H_1 and H_2 holes. The hole at H_1 was located such that the leading edge of the pectoral fin was vertically aligned with the leading edge of the pelvic fin mounted at this location. When fins were not mounted, the body was streamlined by covering the holes for the fins. A 3D-printed block identical to the pectoral fin faring filled the pectoral fin cavity. The pelvic fin holes were smoothed over with molding clay. Similarly, all other openings on the fish body were smoothed over for streamlining during testing. The length of this RMO body was 29.5 cm, which comparable to the standard lengths of typical flying fish listed in Davenport (1992). This length lies within the range of standard lengths of four-winged flying fish of the genus *Cypselurus* which is between 19.25 and 37.8 cm according to Davenport (1994).

Pectoral fin

The pectoral and pelvic fins were designed for fixed wing aerodynamics experiments. Thus, they are designed in the deployed state. Moreover, unlike the fish fins, these fins were designed to remain undeformed under aerodynamic loads. This rigid fin design prevents any fluid structure interactions and allows us to estimate the aerodynamic loads resulting from a specific fin configuration and arrangement. Moreover, the flexural rigidity of the pectoral and pelvic fins are understudied and more information is needed to incorporate a biologically relevant stiffness and stiffness distribution for the fins.

The two primary elements of the pectoral fin presented in this work are the 3D-printed branched skeleton and a silicone membrane. The profile of the pectoral fin was loosely based on the profile of the fin in Deng et al. (2019). The resulting wing span of the RMO from one pectoral fin wingtip to the other was 49.0 cm, each fin having a maximum length of 22.5 cm. This RMO pectoral fin length is within the range of biologically proportional pectoral fin lengths when compared to the length of the RMO. This length is also approximately 76% of the RMO body length, which is less than the maximum pectoral fin length described by Davenport (1992), which is 78–79% of the standard length, required for a flying fish to be able to swim without being disturbed by the size of the pectoral fin.

The pectoral fin skeleton was 3D-printed using a Stratasys Objet 360 printer in VeroWhitePlus material (Fig. 3A). The design approximated the branched geometry of flying fish fin rays. The rays radiated from the pectoral fin faring which could be secured into the pectoral fin cavity. Biological fin rays split into branches several times along their lengths between the fin joint and the outer edges of the fin. For simplicity, the pectoral fin design of the robotic model presented in this paper splits into two branches halfway along the lengths of each ray. Each ray in the RMO pectoral fin was hollow throughout its length except in the smaller branched-off section. Carbon fiber rods of diameter 2 mm were inserted into the hollow printed rays to add stiffness. The leading edge ray (the most anterior one) takes the shape of an Eppler 862 strut airfoil, which is symmetric. The streamlined leading edge profile was critical for keeping flow attached over the wing. The symmetric airfoil shape was chosen to avoid generating a non-zero lift at a zero angle of attack. The rest of the branches were arranged such that the wing skeleton had zero camber.

The main lifting surface of the pectoral fin was the silicone membrane cast from DragonSkin30 SmoothOn silicone. The fabrication process for the pectoral fin is shown in Fig. 3A–D. Figure 3E shows a side view of the wing. The dorsal surface of the silicone fin was flat and the ventral surface was textured by the 3D-printed branches. Between the branches, the silicone was 4 mm thick, while a 1.4 mm coat surrounds the rays on the
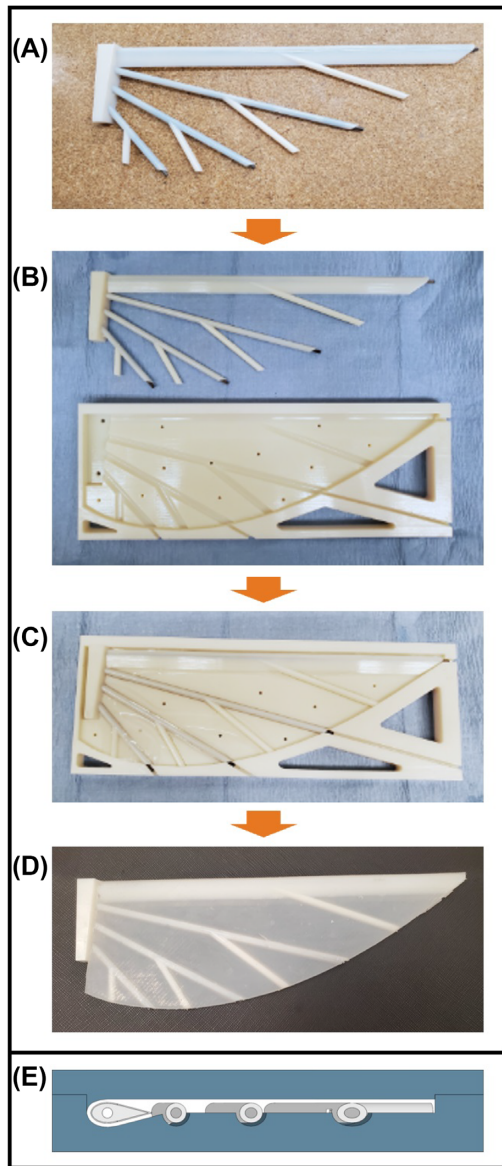
Fig. 3 The silicone molding process. **(A)** The 3D-printed skeleton with carbon fiber rods partially inserted into the hollows of the rays. **(B)** The lower silicone mold is shown adjacent to the wing skeleton, showing the grooves for the rays and girdle block. **(C)** The mold is shown with the skeleton inserted. The grooves in the mold are partially filled with uncured silicone. **(D)** The final cured silicone wing. Note that the carbon fiber rods are now fully inserted into the rays. **(E)** A sectioned side view of the pectoral fin skeleton in the silicone mold. The silicone mold halves are in blue. The white-gray parts are the skeleton. The leading edge airfoil can be seen on the left.

ventral surface. The silicone mold was 3D-printed and composed of an upper and lower half. The upper mold had a depressed surface that defined the thickness of the silicone layer. At the leading edge, this extruded surface contained a curved lip that defined the profile of the fin's leading edge as an offset of the airfoil shape of the 3D-printed leading edge branch. The lower

mold contained a cavity with indentations for the skeleton branches (Fig. 3B). Small through holes were scattered throughout the lower surface of the cavity to provide some relief for the silicone as the upper mold was pressed into place.

The silicone molding process for the fin was as follows:

(1) Forty grams of DragonSkin30 SmoothOn, measured in equal parts A and B, were combined in a Thinky AR-100 conditioning mixer. A 90 s mixing and 120 s defoaming sequence was performed twice consecutively.
(2) The resulting silicone mixture was carefully poured into the lower mold to avoid air bubbles. Only a small amount was initially poured so that the surface of the mold cavity was covered by a thin layer.
(3) The skeleton was pressed into the mold with the carbon fiber rods sticking out slightly from the free end of the rays. The remaining material in the mixing cup was poured over top (Fig. 3C).
(4) The upper surface was situated such that the extruded surface fit within the cavity. Pressure was applied to release silicone through the holes and between the flush surfaces of the upper and lower mold.
(5) The entire system was clamped and inverted to squeeze out the excess material but prevent any more silicone from leaking out of the tiny holes in the lower surface due to gravity.
(6) This was set aside for 24 h at room temperature to cure. Afterwards, the molds were carefully removed, excess cured silicone was cut-off, and the carbon fiber rods were pushed in such that they are flush with the curved surface of the wing. The resulting wing is shown in Fig. 3D.

Pelvic fin

The RMO pelvic fin was composed of a 3D-printed faring, carbon fiber rods, and a ripstop fabric membrane. There is a dearth of anatomical data for flying fish pelvic fins in comparison to pectoral fins. For simplicity, the RMO pelvic fin planform profile was chosen to be the same as that of the pectoral fin at half the scale. The ripstop was supported by 2 mm diameter carbon fiber rods which were directly attached to the fabric surface via ripstop tape and, for the leading edge ray, epoxy. The pelvic fin faring was streamlined to a symmetric airfoil shape whose camber line held a pitch angle $\theta_f = -3°$ relative to the camber line of the pelvic fin (Fig. 2C). The pitch angle of the pelvic fin θ could be varied by joining the pelvic fin faring to the body with an assortment of adapters. The adaptors were designed to induce pitch angle of $\theta = +5°$, $0°$, $-5°$, and $-10°$.

Carangiform-Inspired Caudal Complex

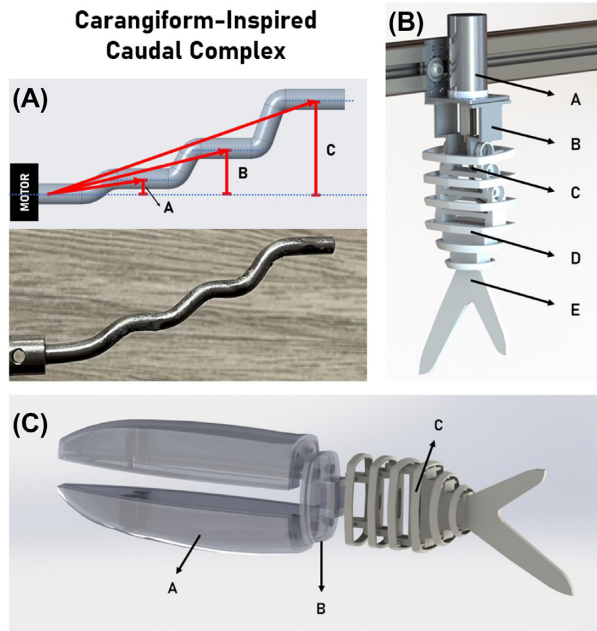**Fig. 4 (A)** Geometry of the stepped axis. (A) $r_1, \theta_1 = 10°$ (B) $r_2 = 3r_1, \theta_2 = 20°$ (C) $r_3 = 6r_1, \theta_3 = 30°$ **(B)** Caudal CAD design layout: (A) motor (B) motor-fin adaptor, only used for testing isolated from the fish body (C) stepped shaft (D) caudal skeleton ribs (E) caudal fin **(C)** Assembly with the fish body: (A) the modified fish body, hollow to house a motor and other controls (B) an adaptor to join the caudal complex to the body (C) the caudal complex.

Caudal complex

The RMO design up until now focused on developing a model for flying fish aerodynamics studies, thus the caudal fin was omitted. Aerodynamics experiments were performed using this design and reported in later sections of this article. However, the design of the RMO was taken a step beyond these experiments to the development of a swimming mechanism based on the caudal complex of flying fish. The design of the caudal complex is included in this section to show the potential of the RMO for evaluating the flying fish performance during swimming and taxiing.

The design of this caudal complex was unique in that it was able to approximate carangiform-like locomotion, as is seen in flying fish, using a cam-and-follower. Inspired by the TunaBot, a continuous rotation motor actuated a shaft that followed slots in the caudal skeleton, which comprised the rib segments and the caudal fin shown in Fig. 4B. Such a mechanism transformed rotational input from the motor into translational motion or a flapping motion at the fin (Zhu et al. 2019). Whereas the TunaBot performed thunniform swimming, our design incorporated a longer stepped shaft (Fig. 4A) that traced out a curved caudal fin profile in order to achieve carangiform locomotion. Additionally, the caudal skeleton was segmented such that there were three points

of rotation along its length. Coupled with the stepped shaft design, this segmentation allowed for a continuous body profile during flapping as observed in carangiform locomotion.

The square-like ribs spanning the length of the caudal skeleton up to the base of the caudal fin were designed to approximate the profile of a flying fish (Breder 1930). The shape of the caudal fin itself was approximated with two asymmetric lobes as seen in Fig. 4. As in a biological flying fish, the dorsal lobe is shorter than the ventral lobe (Davenport 1994). The caudal skeleton was printed using Formlabs Rigid 10K Resin.

$$y = f_B(x, t) = (C_1 x + C_2 x^2) * \sin(kx + \omega t) \qquad (1)$$

The dimensions of the stepped shaft were chosen based on Lighthill's Equation of Fish Motion [equation (1)] where y is the transverse displacement of the tail from the undulation center, x is displacement along the main axis, t is time, k is the body wave number determined by the body length of the fish, ω is the tail beat frequency, and C_1 and C_2 are two carangiform parameters, where $C_1 = 0.5$, and $C_2 = 0.05$ (Kamadulski and Bentsman 2012). Using the maximum recorded standard body length data of different flying fish species (Davenport 1994), equation (1) gives the the average amplitude of the transverse displacement of the caudal complex for flying fish to be 28.4 mm. This value was used when designing the shaft dimensions for the RMO caudal complex design (Fig. 4A). This value can be further supported by calculating the Strouhal number, St, as

$$\text{St} = \frac{fA}{U} \qquad (2)$$

where f is the caudal fin flapping frequency in radians per second, U is the incoming flow speed, and A is the amplitude of a transverse displacement of the caudal fin. The required frequency and velocity data are obtained from observations by Davenport (1994). The flapping frequency during taxiing, which is when the caudal fin flaps the fastest, is reported by Davenport (1994) to be f = 70 flaps per second to achieve swimming speeds near U = 10 m/s. We use the transverse displacement predicted by the Lighthill equation A = 0.024 m. Inserting these values into equation (2) results in a Strouhal number of 0.34. This is very close to the range of the most efficient Strouhal numbers for flapping foils (0.25–0.35) as reported by Kamadulski and Bentsman (2012), thus supporting the the caudal complex and the stepped shaft designs.

Figure 4C shows a CAD assembly of the flying fish RMO including a modified body and the caudal complex. The body in the figure was slightly modified to house the motor and electronics. The body

design could be easily modified to include the cavities for the pectoral and pelvic fins as shown in Fig. 2A.

Experimental design

This section details the experimental procedures for the case studies used to answer the research questions in the article. For both studies, we used an open loop closed section wind tunnel with a test section of 90×45 cm in width and height. The RMO was located in the most upstream section of this wind tunnel where the size of the boundary layer and turbulence was lowest. Figure 2B shows the RMO mounted in the wind tunnel on a sting with a clearance of ~ 20 cm from the wind tunnel floor. All experiments were performed at Reynolds number Re = 30,000, as defined by equation (3), where the free stream speed, $U = 9$ m/s, chord length, $c = 5.2$ cm, and the kinematic viscosity of air $\nu = 15.66 \times 10^{-6}$ Pa s. This Reynolds number was chosen because it is relevant to the Reynolds number of flying fish, which for some species can be found to be Re $\approx 2.0 - 3.0 \times 10^4$ using data from Davenport (1994). The Reynolds numbers for the experiments is closer to the upper limit to maximize the signal to noise ratio for the apparatus used during the experiment.

$$\text{Re} = \frac{Uc}{\nu} \tag{3}$$

A sting, located at center of mass of the RMO, was used to mount the RMO to the wind tunnel experimental setup. The center of mass was determined via CAD software evaluation tools and verified physically with a simple balance check. The sting joins the RMO to a force/torque transducer which is in turn mounted on a motorized gear used to control the RMO body angle of attack, α. Given that the free stream velocity is parallel to the wind tunnel floor, the angle of the sting with respect to the wind tunnel floor defines α. A slot in the floor of the wind tunnel permits the motion of the sting. At each configuration, the force transducer measured forces and moments acting on the RMO, which were resolved to lift, drag, and pitching moments. The force/torque transducer is the ATI Gamma 6-axis force/torque transducer, which has a range of 0–32 N, a resolution of 1/160 N. The force/torque transducer has maximum uncertainties of 0.75% in the x- and y- axes, when measuring at the full scale.

The measured force and moment coefficients are defined using equations (4–6) where L is lift, D is drag, M is pitching moment about the center of mass of the RMO, ρ is the density of air, U is the free stream velocity, S is the planform area of both pectoral fins, and $\bar{c}$ is

the mean aerodynamic chord of a pectoral fin. For our experiments, $\rho = 1.15$ kg/m^2, $U = 9.0$ m/s, $S = 250$ cm^2, and $\bar{c} = 5.2$ cm.

$$C_{\text{L}} = \frac{\text{L}}{\frac{1}{2}\rho U^2 S} \tag{4}$$

$$C_{\text{D}} = \frac{\text{D}}{\frac{1}{2}\rho U^2 S} \tag{5}$$

$$C_{\text{M}} = \frac{\text{M}}{\frac{1}{2}\rho U^2 S\bar{c}} \tag{6}$$

The alignment of the RMO with respect to the free stream in the wind tunnel is critical for obtaining accurate results. The orientation of the fish in the roll direction was fixed by design and the pitching orientation was initially set to zero using an in-house balancing code and later controlled during the experiment to change the angle of attack via the geared motor system. A 3D-printed alignment structure was used to align the yaw orientation. The pegs of the alignment structure fit precisely into the front bolt holes of the prototype and can be moved along square rails on three axes. The alignment system is oriented to the wind tunnel via a small block that fits exactly into a slot on the wind tunnel floor which is known to be in line with the free stream. Once the prototype is aligned, the RMO body bolt is fully tightened and the alignment system is removed.

The experimental procedures described above were used to answer the research question associated with the case study. In the biological validation, we tested the biological relevance of the RMO. For a fixed pelvic fin configuration, we measured the lift, drag, and pitching moment of the RMO at various angles of attack with and without the pelvic fin. We then compared the measured forces and moments to existing literature on the aerodynamic performance of flying fish. In the parametric pelvic fin study, we focused on the effect of the pelvic fin on aerodynamic efficiency and stability. The experimental parameter space included the RMO angle of attack, the pelvic fin pitch angle, θ, and the pelvic location along the body of the fish, H_i (Fig. 2C). The θ is swept through values of -10°, -5°, 0°, and 5°, where negative values indicate a downward pitch angle relative to the body axis. The values for H_i, where $i = 1, 2, 3, 4$, and 5, denote the location of the pelvic fin from the foremost to the aftmost position on the fish body. Each position is approximately one pelvic fin chord length away from adjacent positions. From observation of photos and videos, biological four-winged flying fish will have the pelvic fin located between H_3 and H_5 (BBC 2015; Kamath 2017).

Biological relevance

We evaluate biological relevance by comparing results from our own experiments to previously existing literature on flying fish aerodynamics. More specifically, we compare our lift, drag, and pitching moment results to numerical simulations from Deng et al. (2019) and experiments from Park and Choi (2010). Park and Choi's study is the only experimental aerodynamics study performed on biological flying fish. The fish in that study were not alive and were preserved as in taxidermy. For comparison with the existing data from simulation and experiments, the RMO was studied in three configurations: (1) "two-winged" where only the pectoral fins were mounted, (2) only the pelvic fins were mounted, and (3) "four-winged" where both the pelvic and pectoral fins were mounted. When the pelvic fins were mounted, they were set to $\theta = 0^\circ$ and H_5 as a simple assumption based on true flying fish anatomy. The results for this validation are summarized in Fig. 5.

Starting with the data collected on the RMO designed in this paper, Fig. 5A and B illustrate the additive effects on lift and drag of the pelvic fin, allowing us to compare four-winged flying fish to two-winged flying fish. This effect is expected, as adding the pelvic fins creates new lifting surfaces on the RMO, which increases lift, but also induce a drag penalty (i.e., an increase in drag).

Figure 5C shows the pitching moment coefficient, an important figure when discussing pitching stability, also known as longitudinal stability. Longitudinal stability can be defined as the tendency of the RMO to return to a trim/equilibrium condition, when subjected to a disturbance about the pitching axis. Static longitudinal stability can be assessed by inspecting the pitching moment versus angle of attack plot or the $C_M - \alpha$ curve (i.e., Fig. 5C). An aircraft is considered longitudinally stable if the slope of the curve, referred to as C_{M_α}, is negative and the α-intercept is positive. Under these conditions, if an aircraft is at a negative angle of attack, the negative pitching moment experienced by the RMO would tend to restore the RMO back to the angle of attack where $C_M = 0$, which is the trim condition. Figure 5 shows that an RMO that is only equipped with pectoral fins is not stable. The slope is slightly positive and there is not a well-defined α-intercept. The addition of a pelvic fin is then seen to stabilize the RMO. The four-winged RMO has a more negative slope than the two-winged RMO and has a clear positive α-intercept. Thus, adding the pelvic fins stabilizes the RMO.

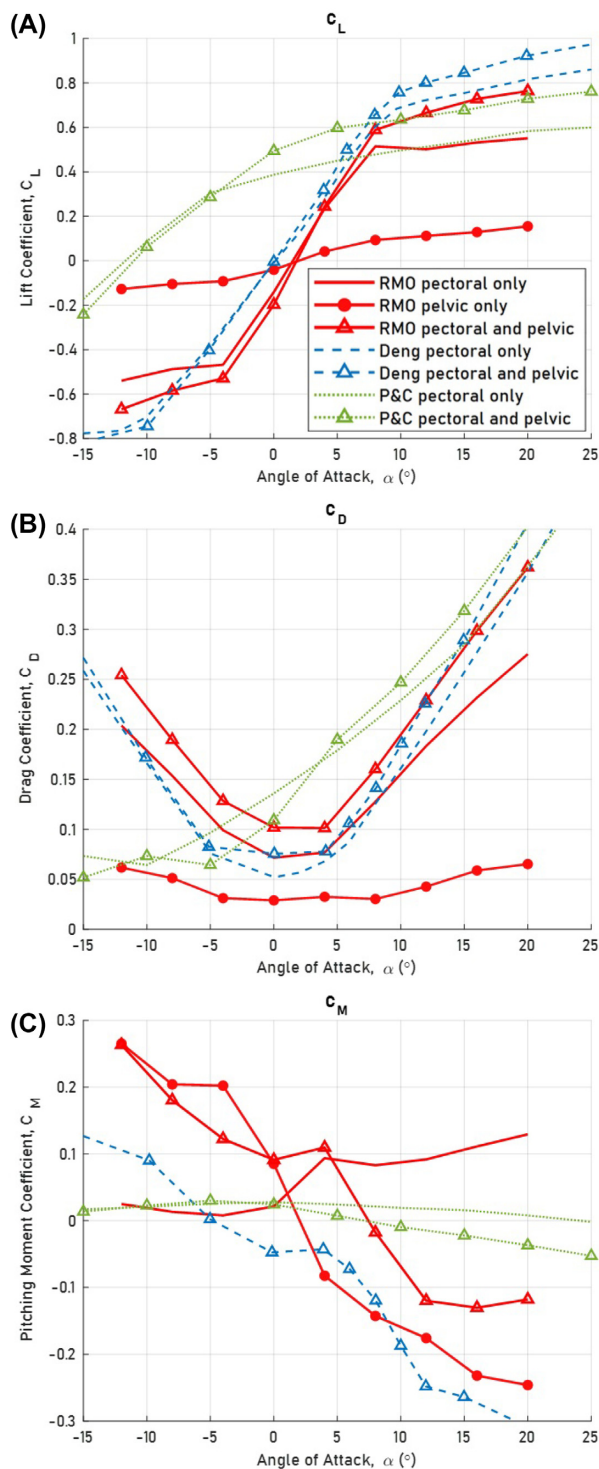The trends observed for the RMO designed in this article can be similarly observed by the results from Park

Fig. 5 (A) The lift coefficient curve. **(B)** The drag coefficient curve. **(C)** The pitching moment coefficient about the center of mass curve versus the body angle of attack for the RMO designed in this study compared to experimental and numerical studies published in the literature. In the legend, "Deng" refers to Deng et al. (2019) and "P&C" refers to Park and Choi (2010).

and Choi (2010) and Deng et al. (2019), which are superimposed in Fig. 5. The addition of a pelvic fin overall increases lift and drag, and improves the longitudinal stability of the fish. The RMO C_L and C_D data (Fig. 5A and B) agree most with the numerical study (Deng et al. 2019). There is notably less agreement with the experimental study on the preserved fish (Park and Choi 2010), especially at lower angles of attack $\alpha < 8^\circ$. This discrepancy can be primarily attributed to differences in fin geometry. The pectoral fins in Park and Choi (2010) have positive pitch angles with respect to the body of the fish of 5° and 7° for the data with with just the pectoral fins and with both pectoral and pelvic fins, respectively. Accounting for this geometrical shift in Fig. 5 would lead to closer agreement between the lift and drag curves of the Park and Choi (2010) and the current study. Moreover, the maximum C_L for the Park and Choi study is lower than the RMO. Such a difference can be attributed to the planform area of the pectoral fins, which is smaller relative to the body of the fish in the Park and Choi (2010) study due to the fins of a preserved fish being more shriveled than those of a living fish in flight (BBC 2015; Kamath 2017).

The C_M data shown in Fig. 5C are more varied between the three studies. This variation can be explained by noting that C_M curves can be very sensitive to the location of the center of mass of each system and to the distance between the center of mass and the neutral point. The neutral point is the point about which C_M would be constant for all angles of attack. Thus, the main purpose of Fig. 5C is to illustrates the proximity of C_M magnitudes to those measured by Deng et al. (2019), and that the pelvic fin is shown to make the slope of the $C_M-\alpha$ curve more negative in all studies. Thus, indicating that the pelvic fin has similar effects on the longitudinal stability of the RMO as has been reported for flying fish.

We have concluded that the RMO produces aerodynamic forces and moments of similar magnitude and behavior as to what is seen in the existing flying fish literature. Moreover, as described in the Design section, the dimensions and geometries of the RMO fins and body are based on biological flying fish. This gives the authors confidence that measurements taken in wind tunnel experiments of this RMO can lend biologically relevant insight into the aerodynamics of flying fish.

Pelvic fin parametric study

After establishing the biological relevance of the RMO, we now shift our focus to understanding the effect of the pelvic fin geometry on the gliding aerodynamics of the RMO. This portion of the current study highlights the advantage of using RMO designs that are modular.

The RMO design allows us to easily change the configuration of the pelvic fin, which enables us to extend the study to configurations beyond those that exist in nature. Such configurations can help uncover evolutionary constraints and design opportunities for engineered systems.

More specifically, we varied the pelvic fin pitch angle, θ, and location along the fish body, H_i. For all configurations, data are reported as the difference between the data with fins and a baseline set of data of an RMO body with no fins. In this study, we focus on two metrics: aerodynamic efficiency and static longitudinal stability. Aerodynamic efficiency is defined as the lift to drag ratio, while static longitudinal stability was defined in an earlier section.

Aerodynamic efficiency

Figure 6 contains a set of main effect plots which report the overall trends in C_L and C_D associated with varying each parameter, namely the RMO angle of attack, the pelvic fin location, and the pelvic fin pitch angle. A main effects plot shows the difference in the mean of a dependent variable (i.e., C_L or C_D) in response to varying different independent variables (e.g., the pelvic fin location). Each plot in Fig. 6 consists of average and upper and lower bounds curves. The average curve represents the mean value of the dependent variable for all configurations at the corresponding independent variable. The lower and upper bounds lines indicate the minimum and maximum values, respectively, such that the shaded region represents the range. For example, in Fig. 6C, for all configurations that have a pelvic fin location of H_5, the average C_L value is ≈ 0.4. At this location, the minimum and maximum values of C_L measured were 0.33 and 0.52, respectively. The goal of main effect plots is to shows whether, on average, a dependent variable responds to changes in the independent variable. If the average curve is horizontal or nearly horizontal, this indicates that the dependent variable is not sensitive or responsive to a given independent variable, or in other words there is no main effect. If the average curve is not horizontal then there is a main effect and the steeper the slope the larger the effect. Thus, Fig. 6 shows the main effects of the RMO angle of attack, pelvic fin location, and pelvic fin pitch angle on lift and drag.

Figures 6A and B show the main effect of the RMO angle of attack on lift and drag. In Fig. 6A, C_L increases at a much slower rate with respect to α in the region where $\alpha > 8^\circ$ than it does where $\alpha < 8^\circ$, indicating the onset of stall near $\alpha = 8^\circ$. The point of stall is not well-defined as is common for wings flying at lower Reynolds numbers. Figure 6B is symmetric about $\alpha = 0$. This is expected because the wings and body are approximately
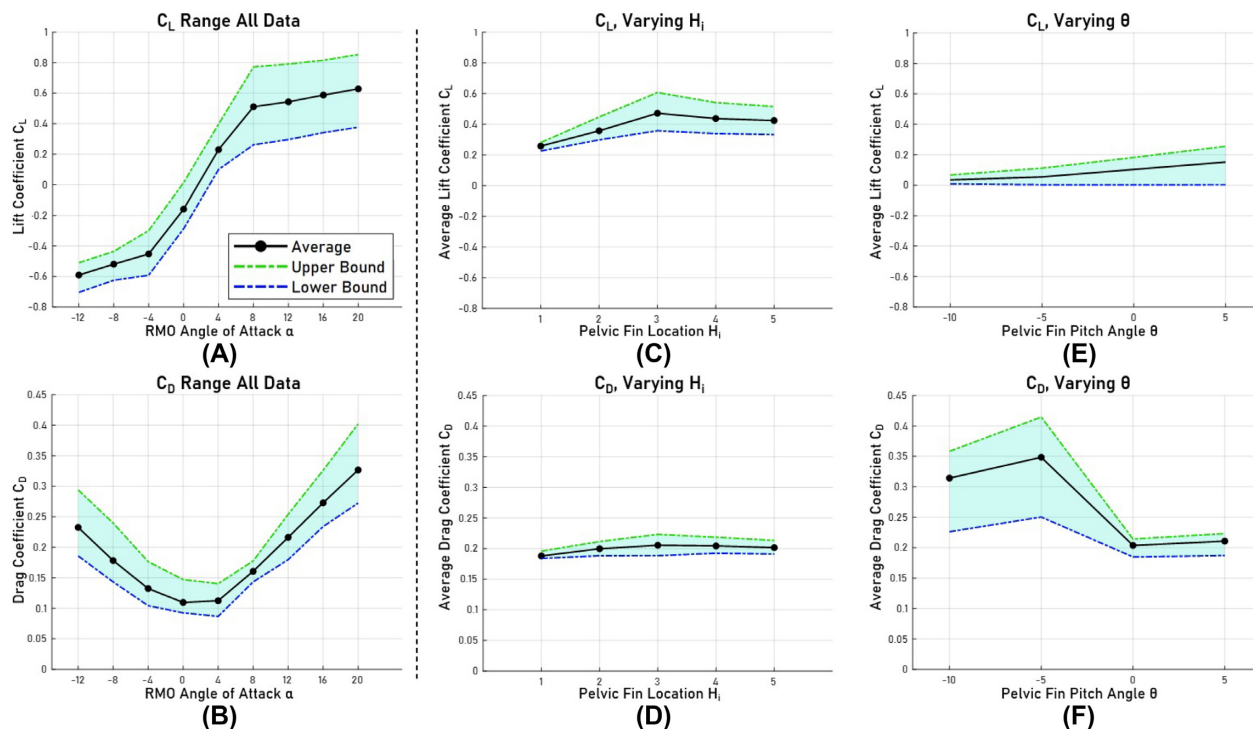
Fig. 6 The black line plots average values. The green and blue dotted lines represent the overall maximum and minimum values respectively. The green shaded area marks the entire range of values for the parameter space. The left two columns represent the lift and drag coefficient curves for all configurations. Each data point in **(C)** and **(D)** is averaged over all θ. Each data point in **(E)** and **(F)** is averaged over all H_i.

symmetric with minimal camber. The RMO angle of attack plots show the typical lift and drag trends for wings and aircraft, further confirming the validity of using the RMO to study the aerodynamics of flying fish gliding. Given the symmetry in the drag curves, the pelvic fin pitch angle and location main effect plots (i.e., Fig. 6C–F) are shown for configurations at $\alpha > 0$ to prevent a loss of effect trends due to symmetry and because flying fish often glide at positive angles of attack where lift is positive.

Figures 6C and E show the main effects of the pelvic fin location and pitch angle on lift, respectively. Moving the pelvic fin farther to the posterior of the RMO tends to increase C_L until the pelvic fin reaches H_3 (Fig. 6C). At this point, the C_L peaks. At H_4 and H_5, the rearmost positions on the RMO body, C_L plateaus at a value slightly less than its value at H_3. Moreover, increasing the pelvic fin pitch angle, θ, increases lift (Fig. 6E). The C_L overall trends to indicate that the pelvic fin is behaving as a lifting surface that produces more lift as the incidence increases. However, having multiple lifting surfaces in close proximity leads to fluid interactions among such surfaces that depends on the spacing between these surfaces. At H_1 and H_2, the pelvic fin is below the pectoral fin. At H_3, the pelvic fin is directly behind the pectoral fin, and at H_4 and H_5, it is staggered

behind the pectoral. Given the location main effects on lift, we hypothesize that the C_L peak experienced at H_3 is due to favorable interactions with the flow immediately behind the pectoral fin. In contrast, the location of the pelvic fin under the pectoral fin, as in the case of the H_1 and H_2 incurrs a lift penalty due to destructive interference between the pelvic and pectoral fin. Finally, at H_4 and H_5, the pelvic fin is far away enough from the pectoral fin that these interactions with the pectoral fin dissipate, reducing the lift compared to the peak location, but improving it relative to locations where destructive interference occurred.

Figures 6D and F show the main effects of the pelvic fin location and pitch angle on drag. The figures show that drag is more sensitive to the pelvic fin pitch angle than to location. Varying H_i does not have a significant impact on C_D (Fig. 6D). In contrast, C_D decreases significantly as θ becomes more positive (Fig. 6F). This change in C_D is unexpected. First, at low speeds, drag is predominately lift-induced drag, and since lift is increasing as θ increases (Fig. 6E), drag should be expected to increase. Another observation in Fig. 6F is that there are wide ranges of values of C_D at the negative angles of attack, but not at the zero and positive angles of attack. This observation can be explained by referencing the previously described differences in the
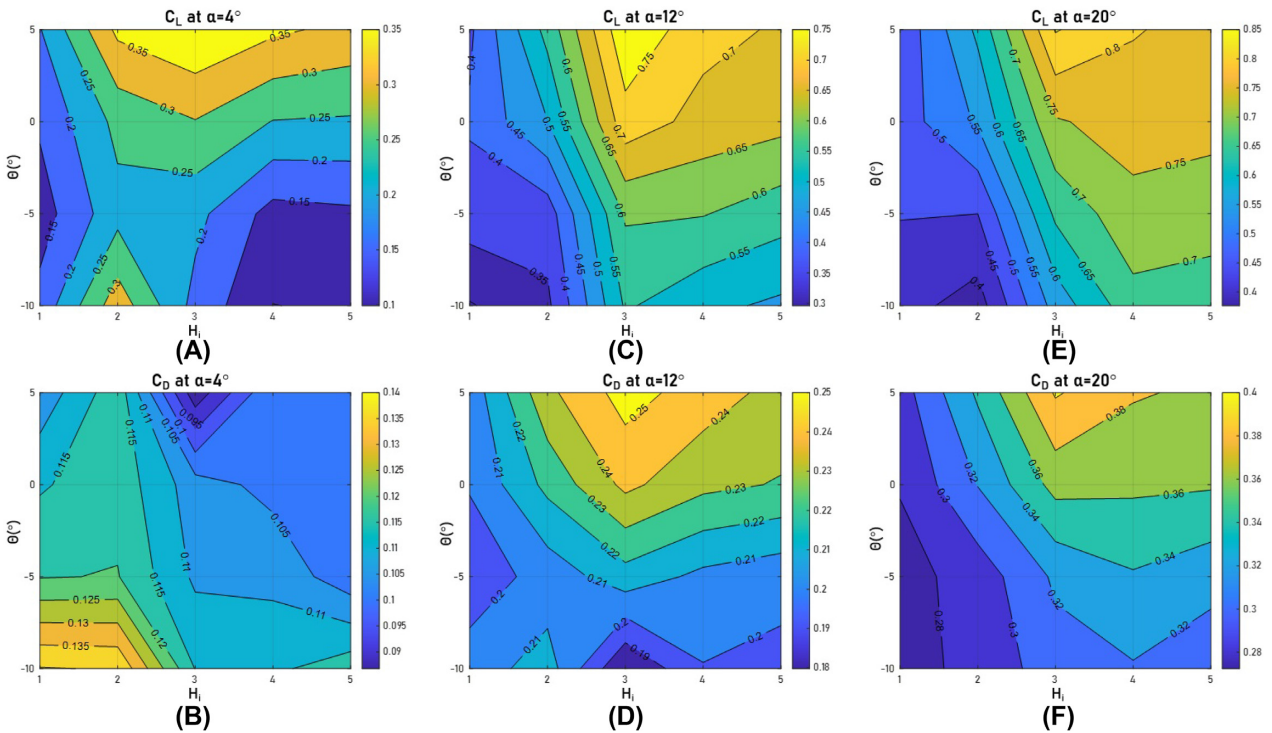
Fig. 7 Each plot shows the C_L (**A**, **C**, **E**) or C_D (**B**, **D**, **F**) over the entire parameter space of the flying fish RMO configurations at a single RMO α. $\alpha = 4°$, $\alpha = 12°$, $\alpha = 20°$ were chosen to represent the trends seen between these coefficients and θ, H_i.

flow field for pelvic fins located immediately below the pectoral fin and those located behind the pectoral fin. We hypothesize that these differences are even more pronounced for drag generated by fins mounted at $\theta < 0°$. A pelvic fin, at H_1 and H_2, and a negative pitch angle, as in Fig. 2C, forms a nozzle-like profile with the pectoral fin, as opposed to a more streamlined profile if $\theta \geq 0°$. The nozzle-like profile would generate higher drag than if the pelvic fin were located at H_3–H_5 where the fins do not form such a profile (Fig. 2C).

These hypotheses about the interactions of the pelvic and pectoral fins can be further investigated by examining contour plots of C_L and C_D at a given α for all pelvic fin configurations tested (Fig. 7). The contour plots show the interactions between the different pelvic fin parameters, which can not be observed from main effect plots. Specifically, results from three α are shown in the contour plots, namely $\alpha = 4°$ (Fig. 7A and B), $\alpha = 12°$ (Fig. 7C and D), and $\alpha = 20°$ (Fig. 7E and F). These angles were selected to represent low and high angle of attack regimes.

First, we examine the observation that C_L increases with α. The contour plots reveal that, for all α, the dependence of C_L on θ varies depending on H_i. This dependence is stronger for the more posterior pelvic fin locations than for the more anterior locations. At locations posterior to H_3, C_L increases with θ. Supporting the hypothesis that starting at H_3 the pelvic fin acts as

an additional lifting surface with favorable or negligible interaction with the pectoral fin. At locations anterior to H_3, C_L increases only slightly from negative to positive values of θ (Fig. 7C and E). This weak dependence on θ or lack thereof at H_1 and H_2 is most easily seen in the $\alpha > 8°$ regime (Fig. 7C and E), but can can also be seen to a lesser extent in the $\alpha < 8°$ regime (Fig. 7A). Once again, these observations support the hypothesis that placing the pelvic fin under the pectoral fin induces strong interactions between both fins and reduces the efficacy of the pelvic fin as an independent lifting surface.

Second, we examine the hypotheses related to drag. Specifically, from the main effect plots, we previously stated that C_D is independent of θ. The contour plots reveal that this statement strongly depends on the flight regime (Fig. 7B, D, and F). While this statement is true for an RMO operating over the entire range of $0° \leq \alpha \leq 20°$, C_D is not independent of θ if we restrict operation within one flight regime. For $\alpha < 8°$, C_D is seen to overall decrease with increasing θ. For $\alpha > 8°$, C_D instead increases with θ. The magnitude of change in C_D is overall higher when varying θ than when varying H_i.

Another hypothesis, formulated from the main effect plots, about drag states that C_D is higher for $\theta < 0°$ than for $\theta > 0°$ (Fig. 6F). While true at low α (Fig. 7B), this is not seen at high α (Fig. 7D and F). We pose that this is

due to the different types of drag experienced at lower versus higher angles of attack. At lower α, skin friction is the main source of drag, while at higher α, induced drag due to maximum lift production or pressure drag due to flow separation tend to be more dominant. Thus, at lower α (i.e., $\alpha = 4^{\circ}$), when the flow is still attached over the pectoral fin and skin friction drag is dominant, the differences in drag are most pronounced between posterior and anterior pelvic fin locations when $\theta < 0^{\circ}$. The drag at $\theta < 0^{\circ}$ is much higher at H_i for $i < 3$ relative to H_i for $i \geq 3$ in Fig. 7B. This trend is again due to the nozzle-like shape that the pelvic fin forms with the pectoral fin at the two most anterior pelvic fin locations. At higher α, higher drag is associated with configurations that produce more lift (Fig. 7D and F). Moreover, at higher α, flow may be separated over some portion of the pectoral fin, thus the drag increase due to the shape of the pelvic fin at negative pitch angles is not observed.

After inspecting the main effects and interactions of the pelvic fin parameters as related to lift and drag, it is important to relate them to a gliding flight performance metric, namely aerodynamic efficiency. Figure 8 shows aerodynamic efficiency, defined as the ratio of lift to drag, L/D for all pelvic fin configurations tested. This figure plots L/D for all pelvic locations H_i as denoted by the legend. Each plot in the figure shows the effect of pelvic fin location for a given pitch angle θ. As the pelvic fin is moved farther aft along the body, the efficiency tends to increase until peaking and plateauing at a maximum efficiency at H_3. Between H_3 and H_5, the efficiency does not significantly change. The efficiency of the RMO is maximized when the pelvic fin is located behind the pectoral fin, but it is not sensitive to its specific location within this region. Moreover, this trend of peak efficiency at H_3 occurs for all pelvic fin pitch angles.

As previously mentioned, biological flying fish pelvic fins are located somewhere between H_3 and H_5. Thus, four-winged flying fish have pelvic fins located along their body such that they reap maximum aerodynamic efficiency in flight.

Longitudinal stability

During gliding, a high aerodynamic efficiency is critical. However, stability is also important. Figure 9 shows the pitching moment coefficient about the RMO center of mass as a function of the RMO angle of attack. Each curve represents a pelvic fin pitch angle, θ and each plot represents a different pelvic fin location, H_i. More specifically, The topmost plot contains the C_M curves for every θ at H_1. Moving down the figure, the plots show C_M curves at each succeeding H_i moving towards the posterior end of the fish through H_5.
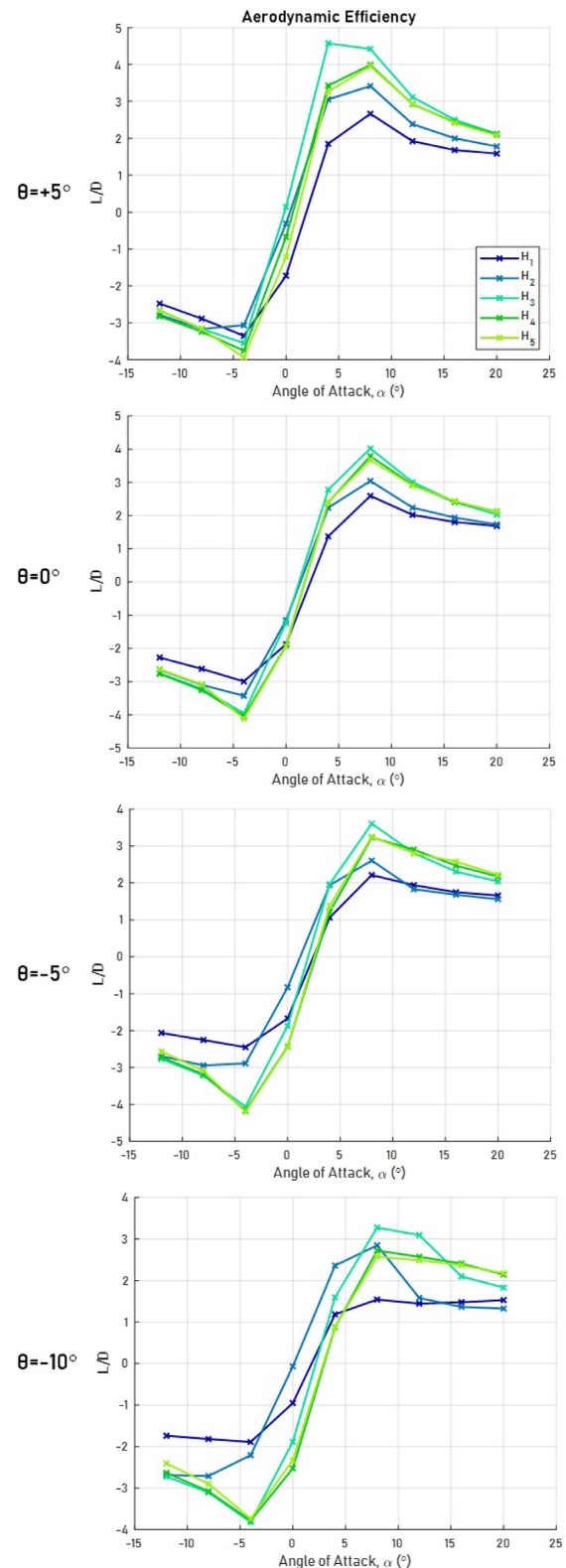

Fig. 8 The aerodynamic efficiency as defined by L/D of the RMO for $\theta = 0^{\circ}$. The topmost figure plots every L/D curve at $\theta = +5^{\circ}$. Each line represents different locations H_i for $i = 1, 2, 3, 4,$ and 5, which are all plotted. Moving down the figure, the plots show L/D for progressively more negative pitch angles θ. Efficiency is seen to be at a maximum for $H_3, H_4,$ and H_5. There is not a significant change in efficiency between these locations.

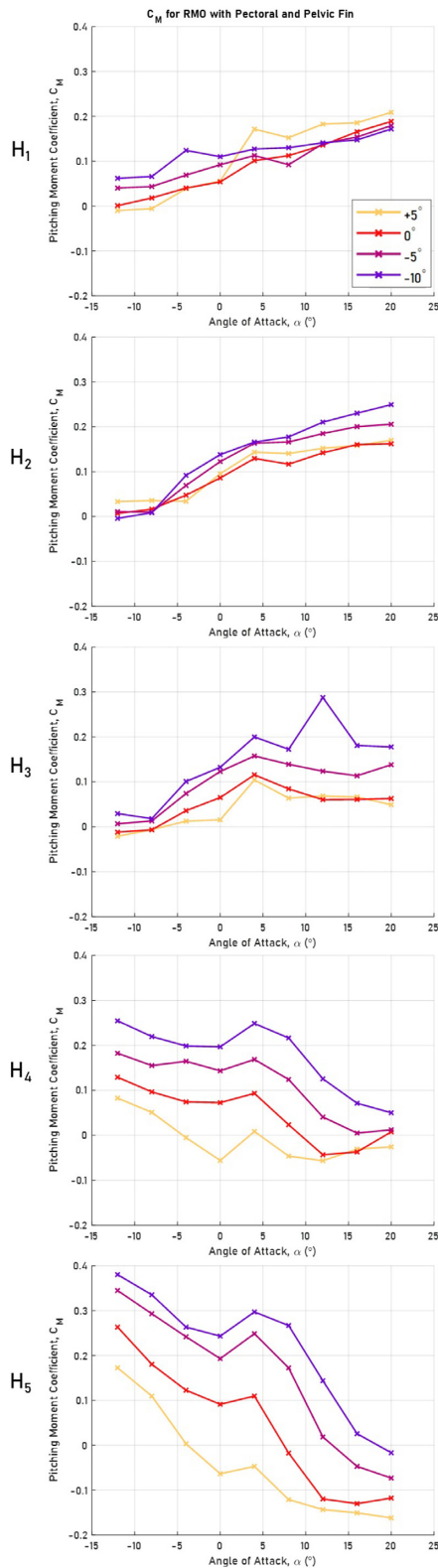**Fig. 9** The topmost figure plots every C_M curve about the center of gravity of the RMO at H_1. The different lines represent different θ. Moving down the figure, the plots represent the C_M at progressively farther aft H_i.

The longitudinal stability of the RMO can be described by both the slope of the $C_M-\alpha$ plot and the intercept on the α-axis. Again, a negative slope with a positive trim point will have a tendency to restore the RMO to the trim point when it experiences a disturbance in the $\pm\alpha$ direction. The RMO is unstable between H_1 and H_3 due to the positive slope and negative trim point. This slope can be seen to become more negative as the pelvic fin is moved farther aft along the fish for all θ. Thus, in general, the RMO becomes more longitudinally stable the more aft the pelvic fin is placed. However, the pelvic fin pitch angle plays a role in determining the location at which the RMO van be considered longitudinally stable. For example, for $\theta = +5°$, the RMO is never stable due to the intercept. At H_4 and H_5, the slope of the $C_M-\alpha$ curve is negative, but the trim point is also negative.

The results illustrate the existence of trade-offs between efficiency and stability within the parameter space of H_i and θ for the pelvic fin. Maximum stability occurs with the pelvic fin at the most posterior location on the RMO, H_5, while the maximum lift occurs at the midpoint, H_3. Simultaneously, maximum lift occurs for the most positive $\theta = +5°$, but all configurations are unstable at H_3. Thus, maximum lift and longitudinal stability cannot be simultaneously independently achieved. While the exact pitch angle of the pelvic fin relative to the body of the fish has not been measured in flight, we can assume that a flying fish benefits from longitudinal stability to maximize gliding time while exposed to disturbances to the free stream prevalent near the air–water interface. Moreover, efficiency is already maximized for any given θ due to the location of the pelvic fin being within the $H_3–H_5$ region. For this reason, we believe it is unlikely that flying fish pelvic fins will have a positive relative pitch angle. However, a flying-fish inspired UAAV may need to be designed for high maneuverability, so a more unstable configuration may be desired.

Conclusions

The flying fish-inspired RMO presented in this paper is an effective tool for studying flying fish gliding flight biomechanics. Using a modular aerodynamics system for wind tunnel experiments, we discovered trends between C_L, C_D, and C_M as functions of the independent pelvic fin variables H_i and θ. We uncovered important insights by investigating aerodynamic efficiency and longitudinal stability as performance metrics during gliding flight. First, as expected, the pelvic fin behaves as an additional lifting surface. Thus, it produces additional lift, increases drag, and shifts the

neutral point or aircraft center of pressure point, affecting longitudinal stability. However, the pelvic fin pitch angle and location change the fin's effect on the aerodynamic forces and moments and dictate the level of interaction between the pelvic fin and the pectoral fin.

The biggest differences in the effects of the pelvic fin on the aerodynamic forces and moments depend on (a) whether the pelvic fin is located just below the pectoral fin at H_1 and H_2 or behind the pectoral fin at H_3–H_5, or (b) whether or not the pelvic fin is at a positive pitch angle. More specifically, the efficiency of the RMO is highest for a pelvic fin located behind the pectoral fin without being sensitive to the specific location within this region. The aerodynamic efficiency was maximum for the intermediate pelvic fin location, H_3, and at a positive fin pitch angle. However, while a positive pitch angle maximized efficiency, it was detrimental for longitudinal stability. Unlike aerodynamic efficiency, the longitudinal stability of the RMO was sensitive to both θ and H_i. The RMO is never stable for $\theta > 0°$. The RMO is also never stable with the pelvic fin located below or just behind the pectoral fin at H_1, H_2, and H_3. Longitudinal stability was only achieved for negative pelvic fin pitch angles and at H_4 and H_5. Thus, there is a clear trade-off between stability and efficiency, where maximum efficiency and stability can not be achieved concurrently.

We found that the operation range of the RMO (i.e., the RMO angle of attack) plays an important role in how the pelvic fin parameters affect drag. Lift trends remained similar over the wide range of operations between $0° \le \alpha \le 20°$. The lift force was more sensitive to the pelvic fin location, with the maximum lift location at H_3, where there was a favorable interaction between the pelvic and pectoral fin. Furthermore, increasing the pelvic fin pitch angle increased lift. Drag, on the other hand, depended on the operation regime. For $\alpha < 8°$, drag was lower for the pelvic fins located behind the pectoral fin than directly below it. This trend was reversed and the dependence diminished for $\alpha > 8°$. The sensitivity of drag trends to the angle of attack was attributed to the type of drag dominating the flow and the pelvic fin parameters. These results are significant when considering the angles of attack or incidence angles that a flying fish will likely experience at different stages of locomotion, as seen in Fig. 1. Flying fish operate at a wide range of angles of attack, ranging from a few degrees during gliding (BBC 2015) to $\approx 30°$ during taxiing and take-off (Davenport 1994). Our results suggest that the flying fish's pelvic fin parameters impact aerodynamic performance differently across different stages of locomotion.

Experiments using the RMO identified trends that are otherwise very difficult or impossible to study on a biological fish. Future studies with flow visualization techniques, either experimental or numerical, will help visualize the aerodynamic interactions between the pectoral and pelvic fins and will uncover the lift and drag production mechanisms as a function of the fin geometric parameters. Using the novel swimming mechanism developed for the RMO, we could perform similar studies focused on the swimming and taxiing locomotion stages. Thus, future use for this RMO design includes conducting hydrodynamics, aerodynamics, and transition experiments to illuminate the fundamental locomotion physics of the flying fish and explore the design of UAAVs inspired by them.

Data availability statement

The data underlying this article will be shared on reasonable request to the corresponding author.

References

Azuma A. 2006. The Biokinetics of Flying and Swimming 2nd edition. New York: Springer.

Flying fish picked off from above and below—The Hunt—BBC Earth, 2015. https://www.bbcearth.com/shows/the-hunt&lang=en.

Breder CM. 1930. On the structural specialization of flying fishes from the standpoint of aerodynamics. Copeia 1930: 114–21.

Davenport J. 1992. Wing-loading, stability, and morphometric relationships in flying fish (*Exocoetidae*) from the northeastern Atlantic. J Mar Biol Assoc UK 72: 25–39.

Davenport J. 1994. How and why do flying fish fly? Rev Fish Biol Fisher 4: 184–214.

Deng J, Zhang L, Zhiyou L, Mao X. 2019. Numerical prediction of aerodynamic performance for a flying fish during gliding flight. Bioinspir Biomim 4: 6–8.

Durnford CD. 1907. The flying fish problem. Am Nat 41: 65–76.

Edgerton H. 1941. High-speed photographs of flyingfishes in flight. Zoologica 26: 311–14.

Fish FE. 1990. Wing design and scaling of flying fish with regard to flight performance. J Zool 221: 391–403.

Flammang BE, Porter ME. 2011. Bioinspiration: applying mechanical design to experimental biology. Integr Comp Biol 51: 128–32.

Franzisket L. 1965. Beobachtungen und messungen am flug der fliegenden fische. Zool Jb(Physiol) 7: 235–40.

Hankin EH. 1920. Observations on the flight of flying fishes. Proc Zool Soc London 90: 467–74

Hertel H. 1966. Structure, Form, Movement. Glendale (AZ): Reinhold.

Photo by Roshan Kamath on Pexels. https://www.pexels.com/photo/flying-fish-1661337/.

Kamadulski S, Bentsman J. 2012. Optimization of biomimetic propulsion in a fish like robot [thesis]. [Illinois (IL)]: University of Illinois at Urbana-Champaign.

Kawachi K, Inada Y, Azuma A. 1993. Optimal flight path of flying fish. J Theor Biol 163: 145–59.

Lucas KN, Lauder GV, Tytell ED. 2020. Airfoil-like mechanics generate thrust on the anterior body of swimming fishes. Proc Natl Acad Sci 117: 201919055.

Makiguchi Y, Kuramochi K, Iwane S, Kojima T, Naito Y. 2013. Take-off performance of flying fish *Cypselurus heterurus* doederleini measured with miniature acceleration data loggers. Aquat Biol 18: 105–11.

Mobius K. 1885. Flying fish do not fly. Nature 31: 192.

Park H, Choi H. 2010. Aerodynamic characteristics of flying fish in gliding flight. J Exp Biol 213: 3269–79.

Rayner JMV. 1986. Pleuston: animals which move in water and air. Endeavor 10: 58–64.

Siddall R, Kovac M. 2014. Launching the AquaMAV: bioinspired design for aerial–aquatic robotic platforms. Bioinspir Biomim 9: 031001.

Zhu J, White C, Wainwright DK, Di Santo V, Lauder GV, Bart-Smith H. 2019. Tuna robotics: a high-frequency experimental platform exploring the performance space of swimming fishes. Sci Robo 4: eaax4615.